Journal of
Synchrotron Radiation

ISSN 0909-0495

Received 18 October 2011
Accepted 28 December 2011

A miniature X-ray emission spectrometer (miniXES) for high-pressure studies in a diamond anvil cell

J. I. Pacold,[a] J. A. Bradley,[b] B. A. Mattern,[a] M. J. Lipp,[b] G. T. Seidler,[a]* P. Chow,[c] Y. Xiao,[c] Eric Rod,[c] B. Rusthoven[d] and J. Quintana[d]

[a]Physics Department, University of Washington, Seattle, WA 98195, USA, [b]Condensed Matter and Materials Division, Lawrence Livermore National Laboratory, Livermore, CA 94550, USA, [c]HPCAT, Carnegie Institution of Washington, Argonne, IL 60439, USA, and [d]APS Engineering Support Division, Argonne National Laboratory, Argonne, IL 60439, USA. E-mail: seidler@uw.edu

Core–shell X-ray emission spectroscopy (XES) is a valuable complement to X-ray absorption spectroscopy (XAS) techniques. However, XES in the hard X-ray regime is much less frequently employed than XAS, often as a consequence of the relative scarcity of XES instrumentation having energy resolutions comparable with the relevant core-hole lifetimes. To address this, a family of inexpensive and easily operated short-working-distance X-ray emission spectrometers has been developed. The use of computer-aided design and rapid prototype machining of plastics allows customization for various emission lines having energies from $\sim$3 keV to $\sim$10 keV. The specific instrument described here, based on a coarsely diced approximant of the Johansson optic, is intended to study volume collapse in Pr metal and compounds by observing the pressure dependence of the Pr $L\alpha$ emission spectrum. The collection solid angle is $\sim$50 msr, roughly equivalent to that of six traditional spherically bent crystal analyzers. The miniature X-ray emission spectrometer (miniXES) methodology will help encourage the adoption and broad application of high-resolution XES capabilities at hard X-ray synchrotron facilities.

Keywords: X-ray emission spectrometer; resonant X-ray emission spectroscopy; high-energy resolution fluorescence detection; volume collapse.

1. Introduction

Core–shell hard X-ray emission spectroscopy (XES) at 1 eV energy resolution is an important technique in condensed matter physics, coordination chemistry, earth sciences and related fields. At such energy resolutions, one obtains very local assessments of the atomic oxidation and spin states and coordination geometry (de Groot, 2005; Glatzel & Bergmann, 2005). Historically, however, a practical limitation has constrained the actual range of applications: few hard X-ray beamlines are equipped to perform high-resolution XES, while many are equipped to perform X-ray absorption spectroscopies. Appreciation for the value of resonant and non-resonant XES and high-energy resolution fluorescence detection (HERFD) has expanded in recent years, with applications in areas including catalysis science (Singh *et al.*, 2010; Yamamoto *et al.*, 2011), biology (Bergmann & Glatzel, 2009), earth sciences (Badro *et al.*, 2004; Lin *et al.*, 2005) and, more generally, identification of ligands (Swarbrick *et al.*, 2010; DeBeer & Pollock, 2011), time-resolved studies (Vanko *et al.*, 2010) and determination of metal oxidation states (Bordage *et al.*, 2011). This growing understanding of the value of XES is driving upgrades of some hard X-ray XAS beamlines to also accommodate regular general access to XES and HERFD, in addition to having such methods included in the conceptual designs for beamlines under construction, such as the inner shell spectroscopy (ISS) and submicron resolution X-ray spectroscopy (SRX) beamlines at NSLS-II.

With some notable exceptions (Hoszowska *et al.*, 1996, 2011; Hayashi *et al.*, 2004, 2008), hard X-ray XES studies at 1 eV energy resolution have used spherically bent crystal analysers (SBCA). These optics are placed $\sim$1 m from the sample, and consequently subtend 8 msr, or about 1/1600 of 4π sr. This relatively small collection solid angle has led to the on-going development of dedicated multi-SBCA spectrometers for resonant and non-resonant XES (Bergmann & Cramer, 1998; Qian *et al.*, 2005; Kleymenov *et al.*, 2011) and for non-resonant inelastic X-ray scattering at similar energy resolutions (Fister *et al.*, 2006; Verbeni *et al.*, 2009). The existence of such instruments, however, is only a partial step towards resolving the shortage of XES and HERFD capability, since each one is usually dedicated to a single

doi:10.1107/S0909049511056081

beamline owing to their construction cost, structural and operational complexity, and overall physical scale.

For the last few years we have been developing a family of portable, inexpensive and easily operated high-resolution hard X-ray spectrometers for use at synchrotron X-ray sources. These short-working-distance (SWD) dispersive spectrometers (Dickinson *et al.*, 2008) make use of arrays of small, flat Bragg analysers placed near the sample. The SWD spectrometers, independent of the optical design, have become known as miniXES ('miniature X-ray emission spectrometers') in the synchrotron community, and we shall use this term in this paper. Our subsequent work on miniXES spectrometers based on the cylindrical von Hámos configuration (von Hámos, 1933) has recently been reported (Mattern *et al.*, 2012). Here, we present and discuss design considerations for instruments based on the Johansson, *i.e.* perfect Rowland circle, geometry. We again use three-dimensional rapid prototype machining and in-context computer-aided design. However, here we use a different, somewhat more flexible, optical configuration and also tailor the design of a particular spectrometer for compatibility with a ubiquitous extreme sample environment: a diamond anvil cell (DAC).

In §2 we summarize the design considerations for Johansson-style miniXES instruments. The general framework for the optimal design of miniXES based on a Rowland circle construction is presented. Such an X-ray optic may be thought of as a coarsely diced approximant to a Johansson bent crystal analyser (Johansson, 1933). In §3 we present design and fabrication details for the Pr $L\alpha$ spectrometer. This instrument is being used in high-pressure DAC studies of Pr metal and compounds where volume collapse is observed, in order to measure concomitant delocalization of the 4f electrons. In §4 we present results for the performance of this instrument, and discuss the generalization of this approach to other energy ranges, systems and sample environments. Finally, in §5 we briefly summarize and conclude.

2. The design of miniXES based on a Johansson configuration

As recently demonstrated (Dickinson *et al.*, 2008), a hard X-ray dispersive spectrometer with 1 eV resolution can be based on a micro-focused beam, a modern two-dimensional position-sensitive detector (2D-PSD), and an array of small, flat Bragg analysers placed a few centimeters from the sample. This approach gives large collection solid angles; for example, a 1 cm^2 flat analyser at 10 cm working distance subtends a somewhat larger collection solid angle than a traditional 10 cm-diameter circular SBCA at 1 m working distance. Here we formalize the design, construction and operation of an important class of such instruments, all with a view towards production of large numbers of miniXES spectrometers of various designs for wide distribution and application in the synchrotron radiation community.

In this section we outline an optimal Rowland circle construction for miniXES-type instruments. By 'optimal', we mean that the dispersed reflections efficiently fill the 2D-PSD surface while retaining unique illumination of each pixel (*i.e.* the dispersed reflections from distinct analyser crystals do not overlap). The design algorithm is described in purely geometric terms, and can therefore be easily implemented in any computer-assisted design (CAD) software that allows geometric constraints. First, in Fig. 1(*a*), we define the correct placement of flat crystals for Bragg angle θ on a Rowland circle of radius R. Note that scattering from the intersection point of any crystal with the Rowland circle comes to a common exit point on the circle. Second, in Fig. 1(*b*), we observe that all virtual sources for flat analysers properly oriented on the Rowland circle must rest on another circle, this one having radius $2R\sin\theta$ and centered about the point P as constructed in Fig. 1(*a*). Third, one may then show a novel result that is closely related to the occurrence of 'dispersion compensation' in SBCA (Huotari *et al.*, 2005), namely that there is a spectral focusing effect along an arc of the circle of virtual sources. As shown in Fig. 1(*b*), independent of where any two Rowland-circle oriented crystals are placed, the scattering from common Bragg angles on their surfaces will necessarily intersect on the circle of virtual sources. This observation leads to the two key results: there is a unique location for an exit aperture that will select the same reflected energy range from each crystal, and Rowland circles for arbitrarily perturbed Bragg angles can be constructed in

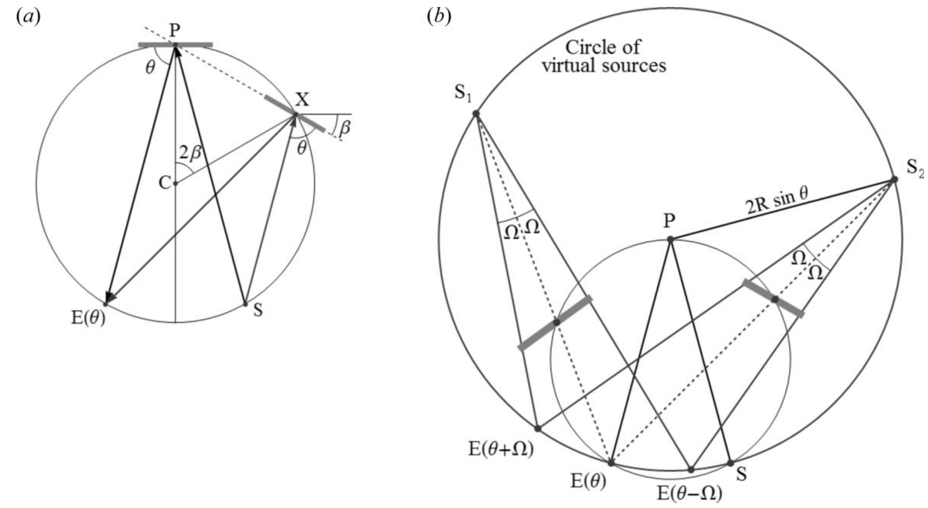

Figure 1
(*a*) The Rowland circle geometry for flat analyser crystals. A crystal placed horizontally through the point P, at the top of the Rowland circle, reflects rays from the source S at Bragg angle θ to the point $E(\theta)$. A flat crystal passing through point X, where the radius CX is at an angle 2β from the vertical, must be tilted by β to reflect at the same Bragg angle. It follows that the crystal lies along the line PX. (*b*) From the observation that appropriately tilted crystals lie on lines passing through P, it is possible to show that the virtual source for reflection from any such crystal lies on a circle of radius $2R\sin\theta$ centered at P. Given a range of Bragg angles, there is an arc on this circle that spatially selects rays reflected in this range from any crystal placed on the Rowland circle.

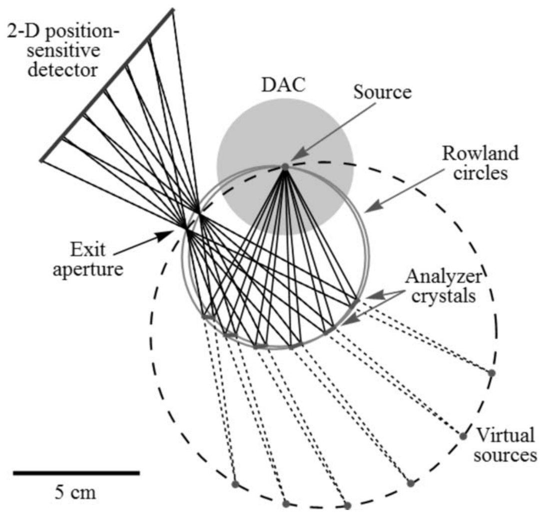

Figure 2
Ray-tracing diagram for a short-working-distance dispersive X-ray spectrometer. Two Rowland circles are constructed through the source point; flat analyser crystals with their endpoints on these circles can be tilted so that they all select the same range of Bragg angles. It then follows (see Fig. 1) that the virtual sources for reflection from the crystals all lie on a third, larger circle (dashed), and that an aperture placed on this circle will select photons in the desired energy range. In this case the position-sensitive detector was located to allow clearance for a 5.6 cm-diameter diamond anvil cell (DAC), and the average diameter of the Rowland circles was approximately 7.4 cm, leaving clearance for a mounting bracket and translation stages (not shown) underneath the crystals.

addition to the original (Bragg angle θ) Rowland circle. In Fig. 1(*b*), these new Rowland circles are defined by the points S, P, and $E(\theta - \Omega)$ for the Bragg angle $\theta - \Omega$ on any crystal, and similarly for Bragg angle $\theta + \Omega$.

With these tools in hand, it is now straightforward to design an optimal Johansson-style miniXES spectrometer for any selected energy range where the detector functions well. We first calculate the required range of Bragg angles, determined by the emission line(s) to be studied and the specific crystal reflection chosen. We then construct the necessary Rowland circles and the circle of virtual sources, and choose a tentative distance and orientation for the detector such that its spatial resolution will yield the desired energy resolution (as discussed in more detail in §4). Iterative ray-tracing between the detector face and the circle of virtual sources (Fig. 2) then provides optimal locations for flat Bragg analysers. We may then gradually modify the Rowland circle radius, and detector location and orientation to satisfy other design constraints (*e.g.* to allow clearance for a DAC as in the present instrument) while also maintaining the desired energy resolution and a substantial collection solid angle. We note that the underlying design can be easily customized for various emission lines, as discussed in §4.

3. Customization for high-pressure studies of Pr *Lα* emission

Several of the elemental lanthanide metals, including Ce, Pr and Gd, but interestingly not Nd, undergo first-order phase transitions at room temperature and high pressure, accompanied by a volume collapse of 5–15% (Zhao *et al.*, 1995; McMahan, 2005; Lipp *et al.*, 2008; McMahan *et al.*, 2009). With the exception of Ce there is an associated change in crystal structure, from high-symmetry transition-metal-like structures at low pressure (*i.e.* structures associated with elements without *f* electrons) to lower-symmetry actinide-like structures at high pressure. This suggests that, in the low-pressure phase, bonding is dominated by the 5*d* electrons and the 4*f* electrons are localized, while in the high-pressure phase the 4*f* electrons become delocalized (Allen & Martin, 1982; Soderlind, 2002). Because of its sensitivity to (i) 4*f* occupation number and (ii) quantum mechanical mixing between the *f* and *d* states, *L*-shell emission spectroscopy is well suited to studying the volume collapse of 4*f* elements. Previous experiments have observed the pressure dependence of the Gd $L\gamma_1$ and $L\alpha$ lines, along with Ce $L\alpha$ (Maddox *et al.*, 2006; Rueff *et al.*, 2006; Rueff & Shukla, 2010).

The present instrument is designed to observe the $L\alpha$ emission spectrum from Pr under high pressure. Consequently, the main design constraint is the clearance required for a diamond anvil cell. The samples in this device are kept between two diamonds to generate GPa-scale pressure and surrounded by a metal gasket (here Be) for confinement. Depending on the target pressure range, typical gaskets are 5–50 µm thick and have a central hole 20–200 µm in diameter. Given these size constraints and the attenuation by the encapsulating material, X-ray emission experiments using SBCA can take hours of exposure to obtain a spectrum at a single pressure point, even at high-flux beamlines (Maddox *et al.*, 2006).

The design methodology of §2 is implemented in the SolidWorks CAD environment. The fixed input parameters are the dimensions of the available 2D-PSD (Dectris Pilatus 100K) and the range of Bragg angles to be collected. The desired energy range (4989–5065 eV) and the crystal reflection Ge (331) give Bragg angles of 70.6–73.2°, which is extended to 70.35–73.45° to provide angular tolerance for the final assembly. Experimentation with the radii of the Rowland circles and the detector distance and orientation resulted in the exact ray-tracing shown in Fig. 2. In the final configuration the collection solid angle is $\sim$50 msr, roughly equivalent to six SBCAs, and the 2D-PSD pixel size (172 × 172 µm) yields $\sim$1.3 eV energy resolution. This sketch is used as the basis for an in-context design of an instrument consisting of a combined spectrometer body and optic, together with an access door. Fig. 3 shows CAD renderings of the spectrometer body constructed to hold the analyser crystals and the entrance and exit apertures, with the ray tracing of Fig. 2 superimposed. Note that the incident X-ray beam (Fig. 3*b*) is parallel to the dispersive direction of the analysers. Most of the miniXES-type instruments that we have built are instead operated with the incident beam perpendicular to the dispersive direction; this makes the spectrometer calibration less sensitive to sample position along the beam. Here, however, experimental constraints imposed by the DAC geometry forced the present configuration.

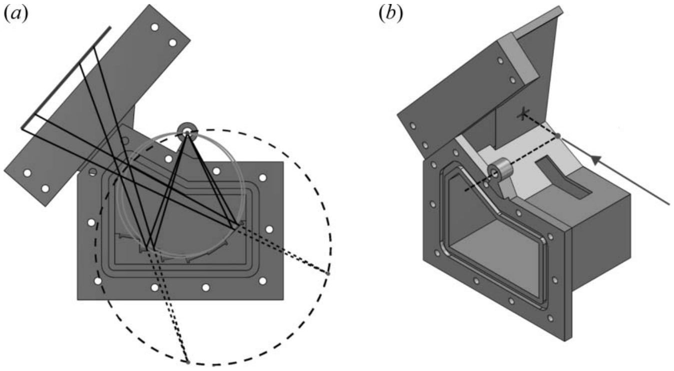

Figure 3
Renderings of the spectrometer body constructed to hold the analyser crystals and X-ray flight path. (*a*) Front view with the ray-tracing from Fig. 1 overlaid; for clarity, the real and virtual rays are shown for reflection from only two of the crystals. (*b*) Isometric view with the incident X-ray beam, the sample point and lines (dashed) to the alignment fiducials. The DAC is omitted.

The plastic spectrometer body was constructed from a thermosetting polymer by an Alaris 30 rapid-prototyping machine (colloquially, a '3D printer'). This has proven to be an efficient and cost-effective way of manufacturing miniXES instruments; we have previously used it to produce Johansson-type spectrometers for the Co $K\beta$ (Kelly *et al.*, 2012), Mn $K\beta$ (Davis *et al.*, 2012) and Ce $L\alpha$ lines (Gordon *et al.*, 2012) in addition to von Hamos-style instruments for the Fe $K\beta$ (Mattern *et al.*, 2012) and Mn $K\beta$ lines (Davis *et al.*, 2012). Profiling measurements have shown that the process holds angular tolerances to within 0.1°. Six Ge (331) crystals are placed on the plastic flats, and the rest of the inner surface is lined with 1 mm-thick Pb tape. Visible in Fig. 3 is a circular hole for rough alignment with the DAC axis, and a cross-hair which is covered with a thin X-ray phosphor film and acts as a rough alignment target for the beam (the incident beam is normal to that face). A window cut in a 0.25 mm-thick Mo plate defines the exit aperture. Work with similar spectrometers has shown that the primary source of background is diffuse scattering of strong sample fluorescence from the analyser crystals and the internal surface of the spectrometer body; to reduce this, two additional 0.25 mm-thick Mo plates are used to define entrance apertures. Each of these plates contains three windows, with each window paired with one of the crystals. This constrains rays entering the spectrometer to illuminate the active region of each crystal (the apertures are oversized by ~20% in each dimension to allow for assembly tolerances). An O-ring-sealed access door, machined from 9.5 mm-thick poly(methyl methacrylate), contains entrance and exit fittings for He flow, installed by standard pipe tap threads. A 9.5 mm machined Al mounting plate fixes the relative positions of the spectrometer body and the 2D-PSD.

Fig. 4 shows the spectrometer installed at Sector 16 of the Advanced Photon Source at Argonne National Laboratory. The spectrometer, 2D-PSD and DAC are mounted on motorized stages to allow reproducible removal and repositioning of each component. This allows the spectrometer and PSD to be translated downstream during adjustments of the DAC pressure.

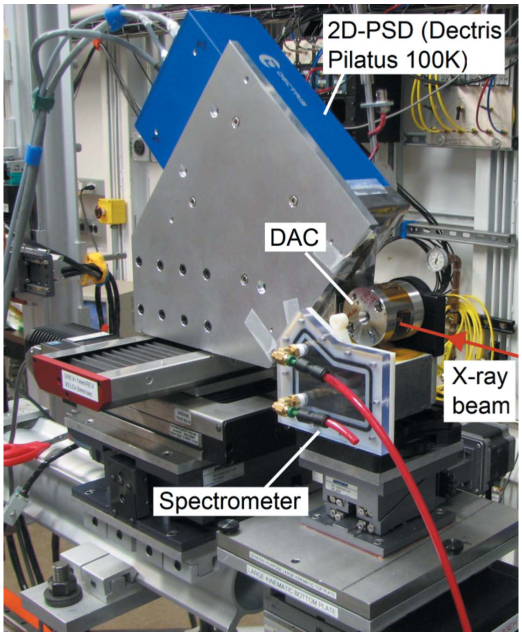

Figure 4
Photograph of the instrument, with the diamond anvil cell and position-sensitive detector in place. For a sense of scale, note that the DAC has a diameter of 5 cm.

4. Spectrometer calibration, results and discussion

Calibration of miniXES instruments for ambient-condition samples makes use of the elastic scattering from the sample itself (Dickinson *et al.*, 2008; Mattern *et al.*, 2012). For DAC-based studies the situation is complicated by the strong elastic scattering from either the diamond or the gasket, depending on the entrance and exit paths for the incident beam. Instead of using the elastic scattering from the target sample itself, the scattering from an ambient reference material (here, a 100 µm-diameter borosilicate glass bead) is used to calibrate the spectrometer. The sample inside the DAC is then placed at the same spatial location to within ~20 µm, ensuring that errors in energy calibration are less than ~0.15 eV. Spatial coincidence of the reference bead and DAC sample is established by standard means based on positioning each on the vertical axis of a rotation stage intersecting the incident beam's focal spot. With the reference bead in place, the incident photon energy is scanned in 7.5 eV steps through the designed energy range for detection of X-ray emission (4989–5064 eV). The monochromator, based on two diamond 111 reflections, has ~1 eV energy resolution in the relevant energy range, and the incident beam profile measures ~30 µm (V) by ~50 µm (H). A 2D-PSD exposure is taken at each step; interpolation between the pixels illuminated at each incident energy (Mattern *et al.*, 2012) produces a map of the photon energy detected by each pixel (Fig. 5).

In the volume collapse study, a sample of pure Pr metal, approximately 150 µm in diameter and 50 µm thick at zero

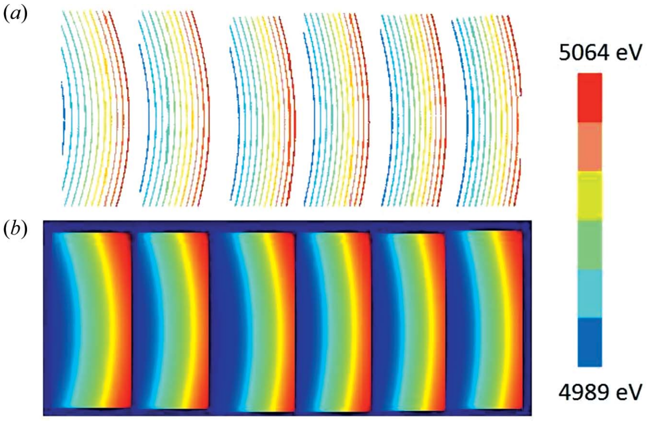

Figure 5
(*a*) A composite image illustrating the calibration procedure. The incident energy was scanned through the detected energy band, and the pixels illuminated on the 2D-PSD were recorded at each incident energy. Note that each crystal illuminates a separate region of the detector. (*b*) Interpolation between these points yields a map of the energy detected at each pixel on the PSD.

pressure, was sealed into a high-purity Be gasket inside the DAC. No pressure medium was used for the data set reported here, as the metal was soft enough to be deformed to fill the hole in the gasket. In addition, this avoided the possibility of chemical reactions at the Pr surface with a pressure-transmitting medium. Spectra were taken at pressures ranging from ambient to 35 GPa and at multiple incident energies near the Pr L_3 edge. Illustrative results are shown in Fig. 6 for $P = 16 \pm 2.5$ GPa, in the general regime required for the transition.

The width of the lines in the elastic exposures used to build the calibration matrix is $\sim$2 eV. Taking into account the resolution of the monochromator, this is consistent with the instrument's intended (purely geometric) energy resolution of $\sim$1.3 eV, and we expect to obtain this resolution when performing non-resonant XES. For resonant XES, on the other hand, the net energy resolution for the experiment would also include the effects of the incident beam's bandwidth (Glatzel & Bergmann, 2005). While the instrument has a collection solid angle roughly equivalent to six SBCAs, overall count rates are low owing to strong absorption of both the incident beam and the fluorescence by the DAC gasket ($\sim$1.5 mm thickness of Be). However, with the incident energy above the Pr L_3 edge (Fig. 6*b*), an integration time of 300 s is sufficient to collect a very low noise $L\alpha$ emission spectrum with an incident flux of 1.6×10^{11} photons s^{-1}. As mentioned above, inelastic scattering of sample fluorescence from the analyser crystals is believed to be the main source of background in miniXES instruments. The problem may be exacerbated in this case by the strong stray scatter of both the incident beam and fluorescence from the Be gasket. Even so, the background is constant to within 3 counts eV^{-1} s^{-1}, and is well below the intensity of the resonant $L\alpha_1$ emission ($\sim$100 counts eV^{-1} s^{-1}). At times, a vanadium chemical filter was used at the entrance aperture to maximize the $L\alpha_1$ signal to (stray scattered) background. Further results on the pressure dependence of the resonant XES from Pr and the issue of volume collapse will be presented elsewhere (Bradley *et al.*, 2012). We note that a separate study used a similar miniXES optical configuration to collect $L\alpha$ emission spectra from Ce compounds (Gordon *et al.*, 2012). The resolution, count rates and low noise levels obtained during these studies show that the miniXES approach is a convenient and effective tool for investigating the physics of *f*-electron materials.

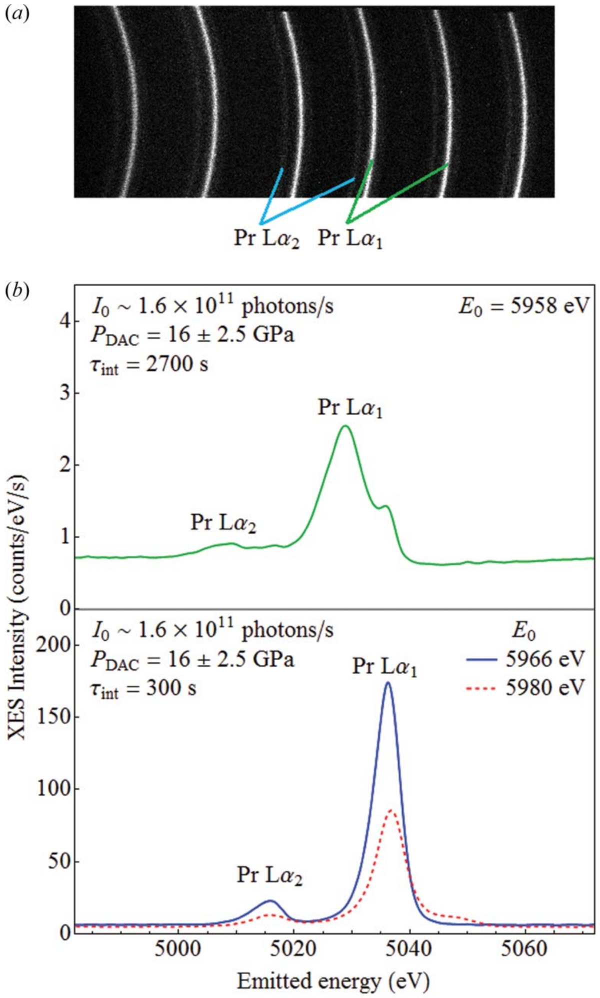

Figure 6
(*a*) A typical image recorded by the 2D-PSD. Several regions corresponding to the Pr $L\alpha_1$ and $L\alpha_2$ emission lines are indicated. (*b*) Processing 2D-PSD images according to the calibration map (Fig. 5) gives the final X-ray emission spectra. Shown here are spectra taken at three incident energies near the Pr L_3 edge (5964 eV), with an incident flux of 1.6×10^{11} photons s^{-1}. Note that resonant Raman scattering features near the $L\alpha_1$ line are resolved.

With the use of CAD software, it is straightforward to modify the underlying design for observation of a wide range of emission lines, subject to the following limitations. First, the 2D-PSD must have sensitivity in the desired energy range and also must have almost zero dark- and readout-noise; exposures at the level of an average of one count of true signal per pixel generate extremely quiet analysed spectra. Second, there must be an appropriate crystal reflection for the desired energy band. By 'appropriate', we mean that the Bragg angles should be close enough to backscatter to allow the desired energy resolution per pixel with a relatively short total distance from sample to the 2D-PSD. To be specific, for photon energies above ~5 keV, the energy resolution is typically dominated by the angular size of a 2D-PSD pixel, as seen from the virtual sources. Since the analyser crystals are dispersive, the detector can be moved farther away to linearly improve the energy resolution, but this also quadratically decreases the collection solid angle. However, as one approaches a 'tender' or intermediate energy range of 3–4 keV, the purely geometric resolution imposed by pixel size becomes more comparable with the intrinsic energy resolution for Si or Ge reflections having a large Bragg angle at the appropriate energy. To summarize, for the Pilatus 100K at 5–10 keV, this means that the Bragg angle should be less than ~20° from backscatter. In addition, given the range of required incident energies, it is necessary to compile a list of other crystal planes that can reflect elastic scattering, Compton scattering or fluorescence from other species onto the 2D-PSD, producing spurious secondary counts. Such interfering planes generally do not exist for high-symmetry analyser crystals (*e.g.* Si, Ge and GaP) and photon energies below 6.5 keV, but at higher energies they may rule out some crystal reflections.

As examples, some viable crystal reflections for the $L\alpha$ emission from each of the lanthanides are listed in Table 1. For specific instruments, additional considerations may apply, *e.g.* the amount of clearance required around the sample and the reflectivity of the possible crystals. Finally, it is crucial to recall that the incident beam must be focused to dimensions somewhat smaller than the pixel size of the 2D-PSD, so that the pixel size is the limiting contributor to the spectrometer's energy resolution. Once the design is finalized, construction and commissioning is conveniently brief. Typically two days of machining time are required for the mechanical support components and Mo shielding, and the rapid prototyping process for the spectrometer body takes roughly a day. After assembly and commissioning, the instrument can be removed and re-installed at the beamline in a few hours, as was the case here.

Before concluding, it is useful to comment on the relative efficiencies of miniXES and SBCA-type systems. Existing miniXES instruments have collection solid angles equivalent to that of 3–10 SBCAs; this approximate range is set by the size of the Pilatus 100K and the distance from virtual sources to the 2D-PSD. This leaves the question of analyser reflectivity. The small size of the analyser crystals used in miniXES typically ensures that one may choose a reflection with the highest theoretical integral reflectivity, which may not be available in a large enough size for manufacture of a complete SBCA. On the other hand, SBCAs sometimes benefit from enhanced integral reflectivity owing to bending-induced strains. These details make direct comparisons between the two approaches problematic. In a recent photometric analysis of a von Hamos-style miniXES instrument, we do find that it performs at the theoretical limit for its design (Mattern *et al.*, 2012). A similar photometric study of typical SBCA-based systems would be quite valuable. As a future direction, we have begun investigating the use of intentionally strained analyser crystals in miniXES spectrometers with an eye to enhancing integral reflectivity.

Table 1
Energies of the $L\alpha$ emission lines of the lanthanides, with corresponding crystal reflections from silicon, germanium and gallium phosphide.

The Bragg angles listed correspond to 20 eV below the $L\alpha_2$ energy and 20 eV above the $L\alpha_1$ energy. Reflections were omitted if both of these angles were less than 70° (*i.e.* if the entire range of Bragg angles selected by the resulting spectrometer would be more than 20° away from backscatter).

Z	Element	$L\alpha_1$ (eV)	$L\alpha_2$ (eV)	Crystal reflection	Bragg angles (°)	
57	La	4651	4634	Ge 400	69.78	71.80
				Si 400	77.82	81.72
				GaP 400	76.87	80.36
58	Ce	4840	4823	Ge 331	79.36	83.97
				Si 400	69.96	71.92
				GaP 400	69.39	71.28
59	Pr	5034	5013	Ge 331	70.92	73.06
				Si 331	79.89	85.21
60	Nd	5230	5208	Si 331	71.39	73.55
61	Pm	5432	5408	Ge 422	79.94	85.09
62	Sm	5636	5609	Ge 422	71.64	73.84
63	Eu	5846	5816	Ge 511/333	76.08	79.23
				Si 422	72.42	74.75
64	Gd	6057	6025	Ge 511/333	69.55	71.47
				Si 511/333	77.43	81.01
				GaP 333	76.50	79.75
65	Tb	6273	6238	Ge 440	80.07	85.48
				Si 511/333	70.48	72.53
				GaP 333	69.89	71.87
66	Dy	6495	6458	Ge 440	72.07	74.33
				GaP 440	80.90	87.76
67	Ho	6720	6679	Si 440	73.34	75.86
				Ge 531	74.12	76.79
				GaP 440	72.64	75.03
68	Er	6949	6905	Si 531	75.70	78.76
69	Tm	7181	7133	Ge 620	74.24	76.99
				Si 531	69.68	71.69
70	Yb	7414	7367	Si 620	76.20	79.30
				Ge 533	75.14	77.96
				Ge 620	68.79	70.61

5. Conclusion

We present a complete design algorithm and methodology for the fabrication of miniXES spectrometers based on the Rowland circle construction. These portable instruments can be quickly installed at any at least modestly focused hard X-ray spectroscopy endstation. To illustrate, we have designed, constructed and commissioned such a short-working-distance spectrometer for resonant XES studies of Pr at high pressures in a standard diamond anvil cell. CAD software was used to preserve the necessary geometry for the analyser crystals while ensuring compatibility with the sample environment. The resulting instrument has low cost, but high collection efficiency and ease of use. The design can be easily modified for studies of other elements. This approach will help spread the adoption of 1 eV resolution XES as a complementary technique to X-ray absorption spectroscopies at hard X-ray beamlines.

GTS acknowledges support of this research program by the US Department of Energy, Basic Energy Sciences, under award DE-SC0002194. This work was performed at HPCAT (Sector 16), Advanced Photon Source (APS), Argonne National Laboratory. HPCAT is supported by CIW, CDAC, UNLV and LLNL through funding from DO E-NNSA, DOE-BES and NSF. APS is supported by DOE-BES, under Contract No. DE-AC02-06CH11357. Part of this work was performed under the auspices of the US Department of Energy by Lawrence Livermore National Laboratory under contract DEAC52-07NA27344.

References

Allen, J. W. & Martin, R. M. (1982). *Phys. Rev. Lett.* **49**, 151106.

Badro, J., Rueff, J. P., Vankó, G., Monaco, G., Fiquet, G. & Guyot, F. (2004). *Science*, **305**, 383–386.

Bergmann, U. & Cramer, S. P. (1998). *Proc. SPIE*, **3448**, 198–209.

Bergmann, U. & Glatzel, P. (2009). *Photosynth. Res.* **102**, 255–266.

Bordage, A., Balan, E., de Villiers, J. P. R., Cromarty, R., Juhin, A., Carvallo, C., Calas, G., Sunder Raju, P. V. & Glatzel, P. (2011). *Phys. Chem. Miner.* **38**, 449–458.

Bradley, J. A., Moore, K. T., Lipp, M. J., Mattern, B. A., Pacold, J. I., Seidler, G. T., Chow, P., Rod, E., Xiao, Y. & Evans, W. J. (2012). *Phys. Rev. Lett.* Submitted.

Davis, K. M., Mattern, B. A., Pacold, J. I., Zakharova, T., Brewe, D., Heald, S., Seidler, G. T. & Pushkar, Y. (2012). *J. Am. Chem. Soc.* In preparation.

DeBeer, S. & Pollock, C. J. (2011). *J. Am. Chem. Soc.* **133**, 5594–5601.

Dickinson, B., Seidler, G. T., Webb, Z. W., Bradley, J. A., Nagle, K. P., Heald, S. M., Gordon, R. A. & Chou, I. M. (2008). *Rev. Sci. Instrum.* **79**, 123112.

Fister, T. T., Seidler, G. T., Wharton, L., Battle, A. R., Ellis, T. B., Cross, J. O., Elam, W. T., Macrander, A. T., Tyson, T. A. & Qian, Q. (2006). *Rev. Sci. Instrum.* **77**, 063901.

Glatzel, P. & Bergmann, U. (2005). *Coord. Chem. Rev.* **249**, 65–95.

Gordon, R. A., Sham, T. K., Mattern, B. A., Seidler, G. T., Stennett, M. C., Reid, D. P. & Hyatt, N. C. (2012). *Phys. Rev. B.* Submitted.

Groot, F. de (2005). *Coord. Chem. Rev.* **249**, 31–63.

Hámos, L. von (1933). *Ann. Phys.* **409**, 716–724.

Hayashi, H., Kawata, M., Takeda, R., Udagawa, Y., Watanabe, Y., Takano, T., Nanao, S. & Kawamura, N. (2004). *J. Electron Spectrosc. Relat. Phenom.* **136**, 191–197.

Hayashi, K., Nakajima, K., Fujiwara, K. & Nishikata, S. (2008). *Rev. Sci. Instrum.* **79**, 033110.

Hoszowska, J., Dousse, J.-Cl., Kern, J. & Rhême, Ch. (1996). *Nucl. Instrum. Methods Phys. Res. A*, **376**, 129–138.

Hoszowska, J., Dousse, J.-Cl., Szlachetko, J., Kayser, Y., Cao, W., Jagodziński, P., Kavčič, M. & Nowak, S. H. (2011). *Phys. Rev. Lett.* **107**, 053001.

Huotari, S., Vankó, Gy., Albergamo, F., Ponchut, C., Graafsma, H., Henriquet, C., Verbeni, R. & Monaco, G. (2005). *J. Synchrotron Rad.* **12**, 467–472.

Johansson, T. (1933). *Z. Phys. A*, **82**, 507–528.

Kelly, S., Bare, S., Pacold, J. I. & Seidler, G. T. (2012). In preparation.

Kleymenov, E., van Bokhoven, J. A., David, C., Glatzel, P., Janousch, M., Alonso-Mori, R., Studer, M., Willimann, M., Bergamaschi, A., Henrich, B. & Nachtegaal, M. (2011). *Rev. Sci. Instrum.* **82**, 065107.

Lin, J. F., Struzhkin, V. V., Jacobsen, S. D., Hu, M., Chow, P., Kung, J., Liu, H., Mao, H. K. & Hemley, R. J. (2005). *Nature (London)*, **436**, 377–380.

Lipp, M. J., Jackson, D., Cynn, H., Aracne, C., Evans, W. J. & McMahan, A. K. (2008). *Phys. Rev. Lett.* **101**, 165703.

McMahan, A. K. (2005). *Phys. Rev. B*, **72**, 115125.

McMahan, A. K., Scalettar, R. T. & Jarrell, M. (2009). *Phys. Rev. B*, **80**, 235105.

Maddox, B. R., Lazicki, A., Yoo, C. S., Iota, V., Chen, M., McMahan, A. K., Hu, M. Y., Chow, P., Scalettar, R. T. & Pickett, W. E. (2006). *Phys. Rev. Lett.* **96**, 215701.

Mattern, B. A., Seidler, G. T., Haave, M., Pacold, J. I., Gordon, R. A., Planillo, J., Quintana, J. & Rusthoven, B. (2012). *Rev. Sci. Instrum.* Accepted.

Qian, Q., Tyson, T. A., Caliebe, W. A. & Kao, C.-C. (2005). *J. Phys. Chem. Solids*, **66**, 2295–2298.

Rueff, J. P., Itié, J. P., Taguchi, M., Hague, C. F., Mariot, J. M., Delaunay, R., Kappler, J. P. & Jaouen, N. (2006). *Phys. Rev. Lett.* **96**, 237403.

Rueff, J. P. & Shukla, A. (2010). *Rev. Mod. Phys.* **82**, 847–896.

Singh, J., Lamberti, C. & van Bokhoven, J. A. (2010). *Chem. Soc. Rev.* **39**, 4754–4766.

Soderlind, P. (2002). *Phys. Rev. B*, **65**, 115105.

Swarbrick, J. C., Kvashnin, Y., Schulte, K., Seenivasan, K., Lamberti, C. & Glatzel, P. (2010). *Inorg. Chem.* **49**, 8323–8332.

Vanko, G., Glatzel, P., Pham, V.-T., Abela, R., Grolimund, D., Borca, C. N., Johnson, S. L., Milne, C. J. & Bressler, C. (2010). *Angew. Chem. Intl Ed.* **49**, 5910–5912.

Verbeni, R., Pylkkänen, T., Huotari, S., Simonelli, L., Vankó, G., Martel, K., Henriquet, C. & Monaco, G. (2009). *J. Synchrotron Rad.* **16**, 469–476.

Yamamoto, T., Nanbu, F., Tanaka, T. & Kawai, J. (2011). *Anal. Chem.* **83**, 1681–1687.

Zhao, Y. C., Porsch, F. & Holzapfel, W. B. (1995). *Phys. Rev. B*, **52**, 134–137.